Computations for Support Design of Measurements of Radiation from Low Velocity Shocked Air

D. A. Levin*
Institute for Defense Analyses, Alexandria, Virginia 22311
R. J. Collins†
University of Minnesota, Minneapolis, Minnesota 55455
and
G. V. Candler‡
North Carolina State University, Raleigh, North Carolina 27695

Hypersonic computational fluid dynamics techniques have recently been used to estimate radiation for vehicles with trajectories in the flight regime of 40 to 60 km altitude and at speeds of about 3.5 km/s. An experiment will be flown shortly to provide the first data to validate these calculations. In this paper, we show how the same computational tools have been used to help in the planning of instruments, primarily for the measurement of optical radiation in the ultraviolet. Theoretical predictions are shown for a sphere-cone vehicle with nose radius of 4 in., at a speed of 3.6 km/s between the altitudes of 40 and 60 km, and are also related to the specific radiometric and spectroscopic measurements planned.

Background and Introduction

THE Innovative Science and Technology Office is in the final planning stages of a sounding rocket experiment. The primary purpose of the experiment will be to measure for the first time optical radiation produced at speeds relevant to exit trajectories. Ground based, shock tube testing[1] has provided good agreement with the computational tools available to date to predict the magnitude of such radiation, which in turn, has allowed us to use these tools with a fair degree of confidence to predict threshold levels of the major optical instruments to be flown. Uncertainties, in the theoretical results, discussed in our companion paper,[2] and differences between the shock tube and space environment, however, should lead to interesting future analyses from such flight data. The important distinction between shock tube and onboard sounding rocket measurements is that the latter provide longer observation times and the presence of a realistic wall temperature which will quickly attenuate the radiation produced in the stagnation region. Moreover, whereas the shock tube radiation levels follow a simple scaling law,[2] the bow shock results do not.

An assortment of onboard spectrometers and radiometers will gather data for altitudes from 40 to 100 km for a vehicle approximated by a sphere-cone shape with a nose radius of 4 in. and a constant velocity from 40 km and higher of 3.6 km/s. Measurements will be taken under nonthrusting conditions. The major optical instruments include a scanning spectrometer with 10 Å wavelength resolution from 1900 to 4000 Å looking forward at the stagnation region through a conformal quartz window of about 1 in. in linear dimension. Various radiometric measurements will also be taken with the intent of providing backup and redundancy measurements to the scanning spectrometer and measuring the radiation levels at angles of 30 and 50 deg relative to the stagnation streamline. The latter measurement will provide data to test the expansion features of the two-dimensional flowfield calculations.[3] An electron microprobe will also be placed in the forward hemisphere to measure electron densities and temperatures. X-band telemetry will be used to relay the measurements back to the anticipated launch site of Wallops Island, Virginia.

The scanning spectrometer and microprobe will be built at the University of Pittsburgh[4] and the final radiometer design and fabrication and total system integration are under the auspices of the program manager at Utah State University.[5]

In an earlier paper[6] the design issues for the above mentioned optical instruments were summarized. Many of these recommendations were carried forward in the instruments that will be flown. The design rationale will be discussed in the section entitled "Experimental Design." Results of calculations undertaken to verify that the final instrument design covers the range of signal levels predicted by theory are shown in the section entitled "Calculations and Final Predictions." These calculations utilized the two-dimensional flow field code of Candler[3] and the radiation code (NEQAIR) of Park.[7] Contributions made with these computational tools to auxiliary instrumentation flight issues related to telemetry and window heating predictions are also discussed.

Experimental Design

Figure 1 shows the final design of the flight vehicle[4] with location and field of view of the optical instruments.

Reference 6 discusses the multichannel signal advantage of a photodiode/image intensifier versus a scanning system. Both systems have about the same sensitivity; but for a 10 Å resolution system, a factor of 40 enhancement can be achieved with the photodiode/image intensification scheme. However, due to dynamic range issues, we suggested the scanning system. The spectrometer final system parameters are very similar to the specifications given earlier.[6] As Fig. 1 shows, the spectrometer will look forward with a 5 deg half angle field of view. Spectrally resolved data, although averaged over variations in temperatures and species concentrations in the field of view, provide information regarding the major radiating species as well as an assessment of the average vibrational temperature. Data bandwidth requirements and space limitations, however, make it impractical to collect spectro-

Received March 28, 1990; revision received Aug. 10, 1990; accepted for publication Sept. 27, 1990.

*Research Staff Member.
†Professor.
‡Assistant Professor.

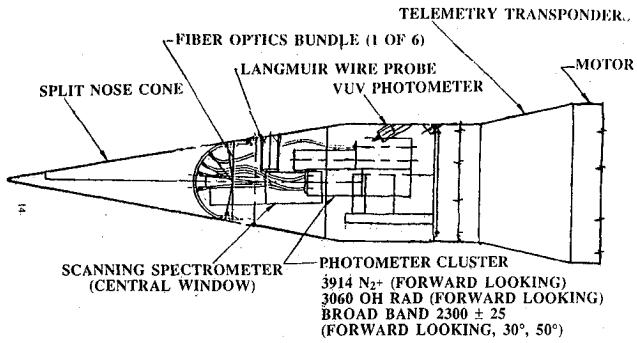

Fig. 1 Design of bow shock rocket experiment.*

scopic data off the stagnation streamline. For this reason, radiometers with optical bandwidths about a factor of 10 larger than the spectrometer resolution will be used to measure radiation in other flowfield locations. The radiometer, a simpler design than the spectrometer, provides important redundancy and confirmation of the latter measurements. As will be shown, the theoretical signal predictions of bow shock intensity at altitudes of about 60 km and higher combined with the spectrometer throughput will give poor signal-to-noise ratios. The broadband radiometric feature should permit measurements with adequate signal-to-noise at the same higher altitudes which is the regime where the flowfield modeling is more uncertain.

The final radiometer design of Espy,[5] although different than discussed earlier,[6] will provide a similar function. The earlier design was based on that flown in the PAET experiment[8] which used a single radiometer. To save space and accommodate the large order of magnitude signal variations a fiber optic and neutral density filter system will be used. This implementation provides seven orders of magnitude dynamic range from the maximum signal level that will not saturate the detectors to the lowest level above the minimum number of counts/s. To accommodate greater dynamic ranges a combination of radiometers may be used with the more sensitive one allowed to saturate at lower altitudes. Figure 1 shows the location of the radiometers and fiber optics and Table 1 provides a summary of their important optical properties.

As discussed in Ref. 6, the radiance calculations obtained from NEQAIR can be combined with standard optical equations[9] to predict the performance of the optical instruments. Since the instrumentation design is final, we have transformed the theoretical results from our usual measure of source radiance expressed in W/cm^2-μsr to counts/s, which, in turn, can readily be converted into counts/channel. Assuming shot-noise limited behavior for the detectors, (which should be a good approximation since the experiment will be flown at night), the power S/N ratio can be predicted.

The number of counts/s, n_c, is related to the bow shock irradiance, I_s, as

$$n_c = \frac{T_w T_{\text{att}} \eta T_c \Omega A_d \int T_f(\lambda) I_s(\lambda) d\lambda}{h\nu} \tag{1}$$

where T_{att} is a product of various signal attenuation factors which were assumed to be unity for the spectrometer. For the radiometer system

$$T_{\text{att}} = T_{f0} T_1 T_{nd} \tag{2}$$

where T_w, T_{f0}, T_1, T_{nd}, are defined in Table 1 and I_s is the source radiance in units of W/cm^2-μsr; T_f is the filter transmission which is a function of wavelength λ. For the spectrometer $T_f = 1.0$. $T_f(\lambda)$ is given in Fig. 4 for the radiometers; A_d is the detector area. For the radiometer it is equivalent to the area of the fiber optic, A_{f0}, given in Table 1. For the spectrometer the appropriate area is that of the slit which is

Table 1 Radiometer and fiber optics properties[5]

T_w,	transmission of dome window, 0.91
A_{f0},	area of 0.01 cm diameter fiber-optic, 7.85×10^{-5} cm^2
Ω	solid angle of fiber-optic, 0.15 sr
$\Delta\lambda$,	bandwidth of filter, ≈60 nm
λ_0,	center wavelength = 234.8 nm
T_{f0},	transmission of fiber-optic, 0.84
T_1,	transmission of collimating lens, 0.91
T_{nd}	transmission of neutral density filter, 0.01
η	quantum efficiency of phototube, 0.12
T_c	counting efficiency, 0.9
t_{int}	integration measurement time, 0.25 s
$n_{\min}$	minimum number of counts/s for ρ = 10, 48 counts/s

Table 2 Scanning spectrometer optical properties[4]

L,	slit length, 1.3 cm
W,	slit width, 0.03 cm
$\Delta\lambda$,	wavelength resolution, 10 Å wavelength range from 1900 to 4000 Å
Ω	solid angle of spectrometer, 0.0239 sr (half angle of 5 deg)
η,	quantum efficiency of detector, 0.3 at 2150 Å
T_w,	dome window transmission, 0.85
T_{att},	instrument transmission, 0.41 at 2150 Å
T_c,	counting efficiency, 0.9
t_{int},	integration time 3.5×10^{-4} s
$n_{\min}$	minimum number of counts/s for ρ = 10, 2.86×10^4 counts/s

the product of LW given in Table 2. The selection of LW conforms to 10 Å resolution[6]; Ω is the device field-of-view solid angle in steradians; h is Planck's constant; ν is the frequency of light.

The remaining two factors, T_c and η, are defined and specified for the radiometer and spectrometer systems in Tables 1 and 2, respectively.

The minimum number of counts/s, $n_{\min}$, required to obtain a specified signal-to-noise ratio, ρ, can be expressed as

$$n_{\min} = \frac{\rho}{2t_{\text{int}}}\left[1 + \left(1 + \frac{4n_d t_{\text{int}}}{\rho}\right)^{1/2}\right] \tag{3}$$

Equation (3) is based on the assumption that for a dark sky background, the significant detector noise sources in the UV spectral range are shot-noise and dark current.[6] n_d and t_{int} are the number of dark counts/s and the measurement time, respectively. Since we require a high degree of confidence in the measured signal value, we used a signal-to-noise ratio of 10. For both instruments it was felt that it would be desirable to have a measurement time that corresponds to 1 km spatial resolution. Thus, for a vehicle moving at 4 km/s this corresponds to a total integration time of 0.25 s which is the value that should be used in Eq. (3) to calculate the minimum required count level for the radiometer. For the spectrometer, however, the measurement time per 10 Å resolution bin is reduced by the time that it takes to sequentially scan from 1900 to 4000 Å as well as the duty cycle of the stepper motor (which moves the grating) and its coordination with the telemetry system.

Calculations and Predictions

The UV transmission at high temperatures can vary significantly among fused quartz window materials. Figures (2a) through (2c) show the expected thermal response of the forward viewing quartz window. High temperature properties such as the absorption coefficient and refractive index of the actual window material, Corning 7940, have not directly been measured; estimates were obtained from related materials.[10] To protect the window from excessive heating a protective nose cone constructed of a honeycomb graphite-aluminum sandwich structure will be ejected between 35 and 40 km altitude. Figure 2a shows the transient and steady-state temperature behavior for the front and back surfaces of the window as a function of time from initial exposure. Freestream

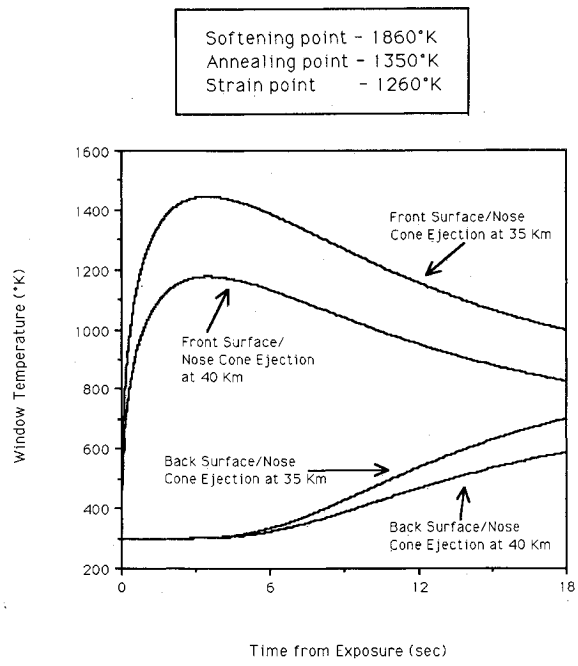

Fig. 2a Corning 7940 window response as a function of exposure time.

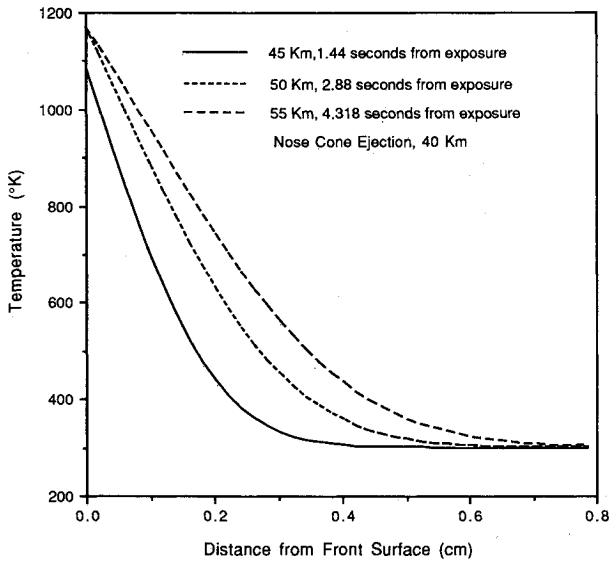

Fig. 2b Temperature profiles through Corning 7940 fused silica.

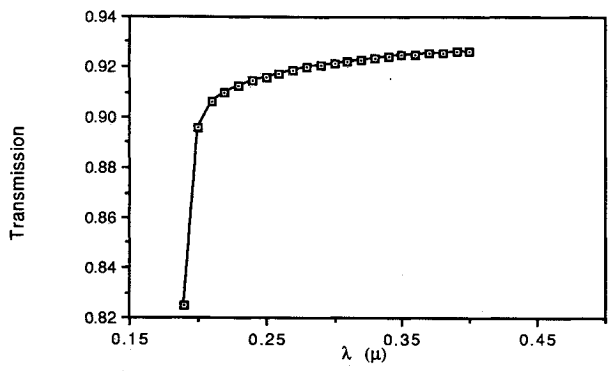

Fig. 2c Corning 7940 transmission as a function of wavelength.

conditions of the anticipated vehicle trajectory were used in a transient heat condition analysis[11] to compute window temperature profiles. For ejection at 40-km temperatures are below critical material properties, with a potentially more serious situation if ejection occurs earlier. Figure 2b, however, shows that only a small depth of material will be at elevated temperatures. Using one of the thermal profiles shown in Fig. 2b with absorption coefficient and refractive index estimates from Ref. 10, the transmission through the window is shown as a function of wavelength. The figure shows that there will be high transmission in the spectral range of interest, thereby, confirming the choice as UV grade sensitive window material.

Figure 3 shows the grid used in the flowfield calculations for a sphere-cone vehicle with nose radius of 4 in. at a speed of 3.6 km/s. The placement of the optical instruments with their corresponding fields of view relative to the grid is also shown for the spectrometer and two 230-nm radiometers. Examination of contour plots of radiation levels showed that grid points from radial lines adjacent to the centerline of each fiber optic, encompassed in the field of view, are basically in the freestream. Therefore, only a single radial line effectively contributes to radiation falling onto the fiber optic for the radiometer field of view corresponding to a half angle of 12.7 deg and the fiber optic diameter of 100 μ. The grid chosen to perform the calculation, however, is felt to be adequate since examination of the total integrated radiation along each of the 55 radials shows a slowly varying function. Since the points that contribute significantly to the radiation falling on the fiber optic essentially subtend the same solid angle from the detector, a constant value of Ω equal to 0.15 sr was used. The spectrometer entrance slit is located about two nose radii along the stagnation streamline and has a half angle field of view of 5 deg, as is also shown in Fig. 3. Spectrally, resolved radiance values were averaged over the six radials that are encompassed by the spectrometer field of view. As before, the points that fall within the field of view and effectively contribute to the total radiation that enters the monochrometer subtend essentially the same solid angle relative to the slit.

Figure 4 presents a comparison between the laboratory measured transmission ("Calibrated Filter") of the filters used with the 230 nm radiometers and a gaussian filter function fit to that data that was used in NEQAIR. The filter center is at 234.8 nm with a maximum transmission of 26.8% and an optical bandwidth of 50 nm. The gaussian approximation is good in the peak transmission regions of the filter with some error introduced in the tails. The choice of the above center wavelength is to cover the peak radiating region of the NO(γ) bands.[2]

Figure 5 shows the theoretical prediction of signal counting levels as a function of location in the shock layer at 40 km. Also indicated are the location of the fiber optics at 30 and 50 deg for the 230-nm radiometers. The results are obtained by superimposing the filter function shown in Fig. 4 over the radiance integration given in Eq. (1) above. The limits of the wavelength integration are from λ = 1600 Å to 3200 Å with an average $\Delta\lambda$ of .6 Å. Contour levels are given in terms of counts/s/cm since this is a graphical representation of signal levels at each point in the radiation field. Examination of the figure shows that the maximum radiation levels are close to the body. Similar spatial dependence of radiation is observed at high altitudes with corresponding absolute magnitude decrease in radiation of many orders of magnitude.

In Fig. 6 the radial integration is performed enabling a plot of counts/s observed through the 230-nm filter as a function of angle from the stagnation streamline for 40, 50, and 60 km altitude conditions. The experimental implementation applies to the values at 0, 30, and 50 deg only; however, presentation of the calculations in this manner illustrates some interesting trends. The ratios at 0, 30, and 50 deg in signal levels are similar for the 40 and 50 km solutions. At 60 km, however, there is a faster dropoff in signal levels off axis. Also indicated

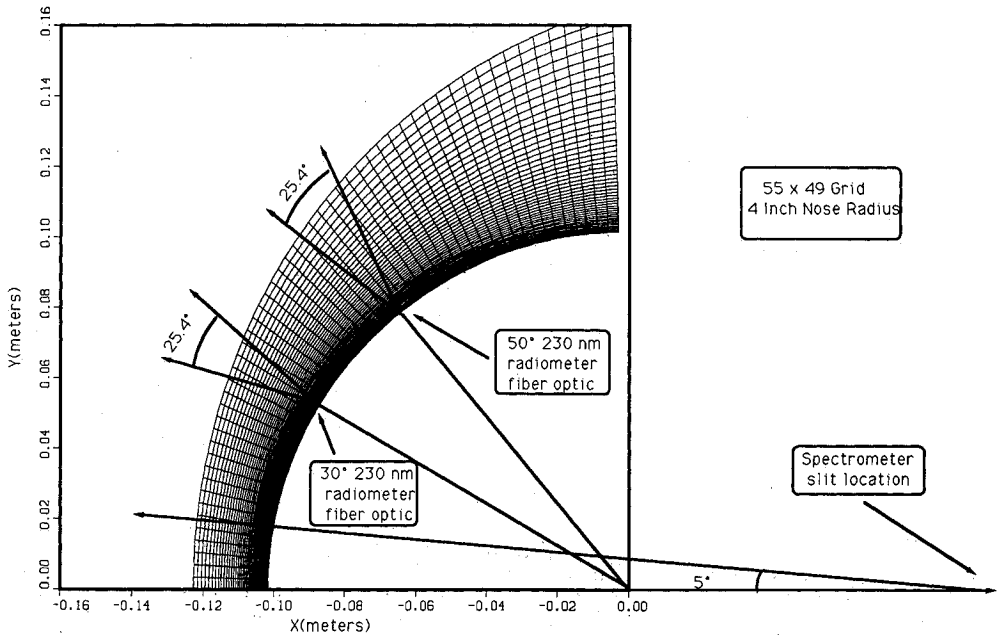

Fig. 3 Optical instruments fields of view superimposed on computational grid.

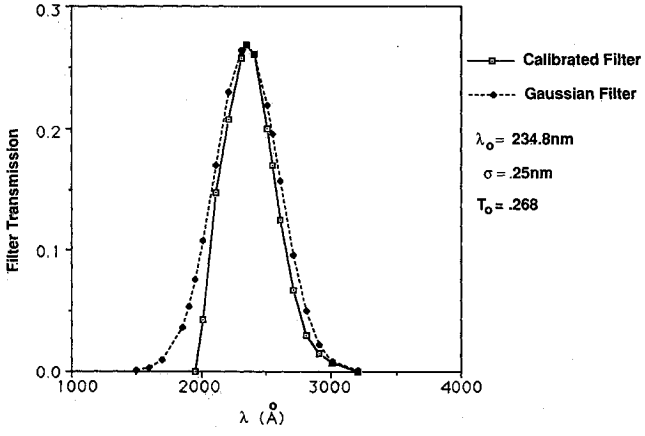

Fig. 4 Comparison of calibrated vs modeled 230 nm filter transmission values.

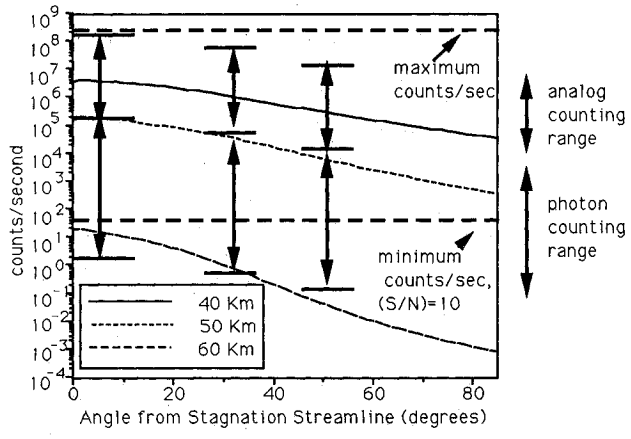

Fig. 6 Prediction of 230 nm radiometer response as a function of location off axis for 3.6 km/s, 4 in. nose radius.

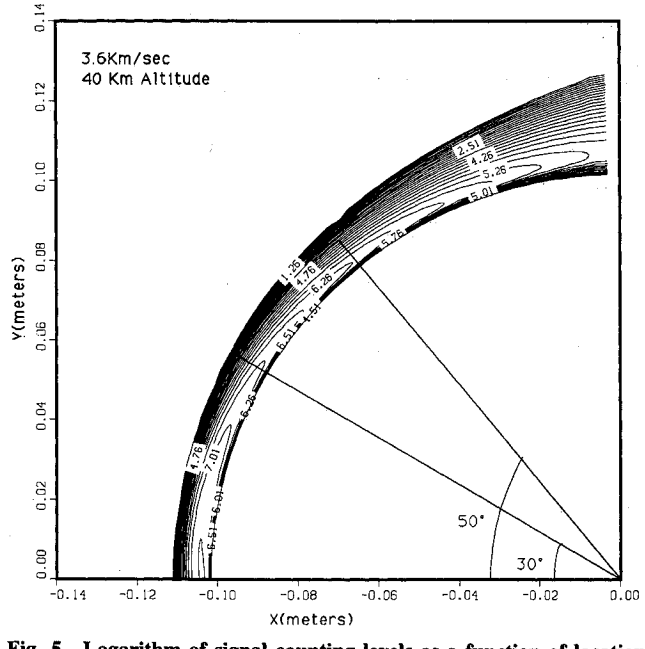

Fig. 5 Logarithm of signal counting levels as a function of location in the shock layer.

on the figure are 230-nm detector characteristic. The solid line at a value of approximately 48 counts/s represents the minimum number of counts/s required to obtain a signal-to-noise ratio of 10. The two sets of vertical arrows, at 30 and 50 deg, show the dynamic ranges permissible with analog and photon counting modes.[5] The upper limit of the analog counting mode will be set to be a factor of 50 greater than the theoretical prediction at 40-km altitude for each respective angle. It is possible that nose cone ejection will occur at a lower altitude than 40 km. This factor then represents a safety margin to avoid detector saturation. For a given radiometer the maximum total dynamic range of the detector is the sum of the analog and photon counting modes, i.e., eight orders of magnitude. However, due to noise limitations and predicted drop off of the signal at 60 km, we effectively obtain six orders of magnitude dynamic range. Also there is an effective maximum count level which is shown in Fig. 6. It is obtained from calibration of the saturation properties of the detector. Again the prediction of the device response is made assuming the use of a neutral density filter with 1% attenuation and a fiber optic diameter of 100 μ. For the 30 and 50 deg cases, we initially considered removing the neutral density filters and using a 400 μ diameter fiber optic (which are readily available) to achieve an overall improvement of 1600 in sensitivity. While this would achieve the sensitivity required at

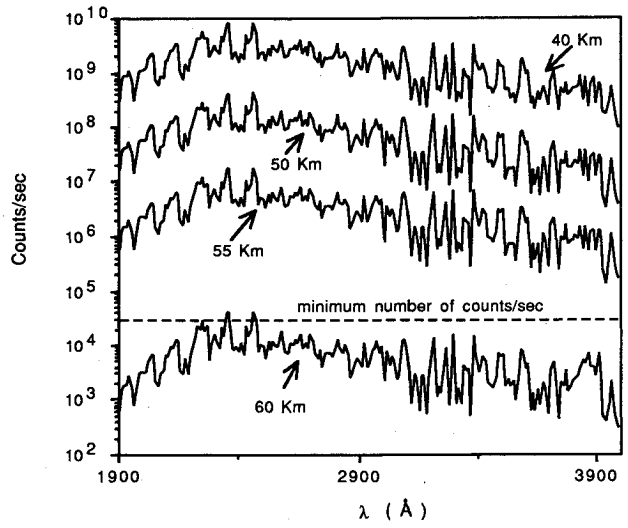

Fig. 7 Prediction of spectrometer response as a function of altitude.

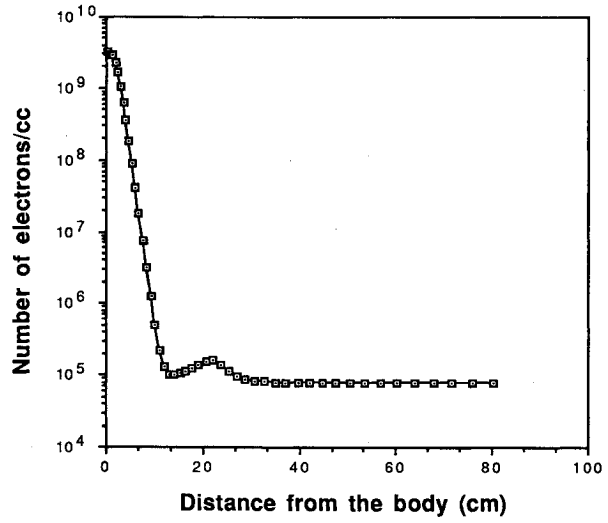

Fig. 8 Electron concentrations for test vehicle at 40 km altitude, 3.5 km/s at the telemetry transponder location.

high altitudes (60 km), the low-altitude signal level would exceed the maximum signal level constraint. This in turn could cause severe detector saturation initially (at 40 km) with insufficient recovery to measure the high altitude signal levels. Hence, if the modeling is correct, it is likely that the off-axis, high-altitude radiance levels will be unmeasurable in this experiment.

Figure 7 shows the predicted signal levels of the scanning spectrometer in the region of the NO(γ) bands as a function of altitude. Imposing the noise limited criterion of approximately 2×10^4 count/s, it can be seen that somewhere between 55 and 60 km altitude there will be insufficient signal. Since data will be available at a spatial resolution of about 1 km, it should be possible posttrial to add signal to obtain spectra at a coarser altitude resolution. Also the forward radiometer shown in Fig. 1 should provide adequate sensitivity at the higher altitudes.

As mentioned above, we also examined the possibility of plasma sheath blackout which is of important concern since there is no onboard data recording capability or posttrial payload recovery. Figure 8 shows the electron density as a function of distance from the body to the radial location aft of the body where the X-band telemetry antennas are located (see Fig. 1). The flowfield calculation was carried out for a 4-in.

Table 3 Radar signal attenuation calculation

radar frequency, 2269.5 Mhz
electron temperature, <2000°K
Predominant species is N_2, σ_e-N_2·$nN_2 \approx 1$ for an electron-molecular N_2 inelastic excitation cross section on the order of 1 Å^2
$N_e < 10^{10}$e$^-$/cm^3, for about 20 cm.

nose radius sphere-cone shape at an altitude of 40 km and a speed of 3.5 km/s. The assumptions made in the calculations were a noncatalytic wall, which tends to raise electron densities, and the lack of any additional shock formation due to the presence of the hinge at the sphere-cone juncture. The degree of radar signal attenuation is a function of the density of electrons, inelastic cross section of prominent species with electrons, gas temperature, and radar frequency.[12] Table 3 shows the values used in the calculation. Approximately a 0.2 dB loss in power was calculated which is negligible relative to the 20 dB power tolerance in the telemetry design.[13] High-altitude cases were not examined since electron densities and temperatures would decrease relative to 40 km and 3.5 km/s conditions.

Conclusions

The above calculations and results have provided real time input to a planned on board experiment which will predominantly measure optical radiation in the ultra violet. The calculations have been helpful in setting optical threshold and saturation levels as well as dynamic range requirements in the final planning stages of the experiment. It is recommended that instrumentation for future experiments in this flight regime be developed and tested with more favorable detector saturation characteristics that would permit greater measurement dynamic range. Close coordination between modelers and instrumentation designers provides high probability of mission success and future interesting analyses.

Acknowledgments

This research is supported by SDIO/IST managed by the Army Research Office under contract MDA 903-89-C-0003. We would also like to acknowledge the Computational Chemistry Branch of NASA Ames Research Center for providing supercomputer time.

References

[1]Wurster, W. H., Treanor, C., and Williams, M., "Non-equilibrium UV Radiation and Kinetics behind Shock Waves in Air," AIAA-89-1918, 1989.

[2]Levin, D. A., Loda, R. T., Candler, G. V., and Park, C., "Theory of Radiation from Low Velocity Heated Air," AIAA-90-0133, Jan. 1990.

[3]Candler, G. V., and MacCormack, R., "The Computation of Hypersonic Ionized Flows in Chemical and Thermal Non-equilibrium," AIAA-88-0511, 1988.

[4]Zipf, E., and Erdman, P., "Bow Shock Ultra Violet Emission Flight Experiment Critical Design Review," 17 Aug. 1989, Space Dynamics Laboratory SDL/89-075.

[5]Espy, P., and Howlett, C., "Bow Shock Ultra Violet Emission Flight Experiment Critical Design Review," 17 Aug. 1989, Space Dynamics Laboratory SDL/89-075, pp. 98–108.

[6]Levin, D. A., Loda, R. T., and Collins, R. J., "Instrumentation Considerations for a Bow Shock Radiation Experiment," *Space Sensing, Communications, and Networking*, Vol. 1059, Society of Photo-Optical Instrumentation Engineers, 1989, 226.

[7]Park, C., "Calculation of Non-equilibrium Radiation in the Flight Regimes of Aero-Assisted Orbital Transfer Vehicles," Thermal Design of Aero-Assisted Orbital Transfer Vehicles, edited by H. F. Nelson, *Progress of Astronautics and Aeronautics*, Vol. 96, 1985.

[8]Whiting, E. E., Arnold, J. O., and Reynolds, R. M., *Journal of Quantitative Spectroscopy and Radiative Transfer*, 13, 837 (1973).

[9]Kingston, R. H., *Detection of Optical and Infrared Radiation*, Vol. 10, Springer-Verlag, New York 1978.
[10]Desai, P. D., Bogaard, R. H., and Chaney, J. F., "Thermophysical and Optical Properties of Corning Code 7940 Fused Silica," HTMIAC Special Report 37, Jan. 1990.
[11]Anderson, J. D., Jr. *Hypersonic and High Temperature Gas Dynamics*, McGraw-Hill, New York 1989, pp. 228–291.
[12]Martin, J. J., *Atmospheric Reentry*, Prentice-Hall Space Technology Series, 1966, pp. 126–128.
[13]Smith, G., Space Data Corp., see Ref. 4 pp. 144–181.